

Effects of fluorinated solvents on electrolyte solvation structures and electrode/electrolyte interphases for lithium metal batteries

Xia Cao^{a,1}, Peiyuan Gao^{b,1}, Xiaodi Ren^{a,2}, Lianfeng Zou^c, Mark H. Engelhard^c, Bethany E. Matthews^a, Jiangtao Hu^a, Chaojiang Niu^a, Dianying Liu^a, Bruce W. Arey^a, Chongmin Wang^c, Jie Xiao^a, Jun Liu^a, Wu Xu^{a,3}, and Ji-Guang Zhang^{a,3}

^aEnergy and Environment Directorate, Pacific Northwest National Laboratory, Richland, WA 99354; ^bPhysical and Computational Sciences Directorate, Pacific Northwest National Laboratory, Richland, WA 99354; and ^cEnvironmental Molecular Sciences Laboratory, Pacific Northwest National Laboratory, Richland, WA 99354

Edited by Alexis T. Bell, University of California, Berkeley, CA, and approved January 8, 2021 (received for review September 29, 2020)

Electrolyte is very critical to the performance of the high-voltage lithium (Li) metal battery (LMB), which is one of the most attractive candidates for the next-generation high-density energy-storage systems. Electrolyte formulation and structure determine the physical properties of the electrolytes and their interfacial chemistries on the electrode surfaces. Localized high-concentration electrolytes (LHCEs) outperform state-of-the-art carbonate electrolytes in many aspects in LMBs due to their unique solvation structures. Types of fluorinated cosolvents used in LHCEs are investigated here in searching for the most suitable diluent for high-concentration electrolytes (HCEs). Nonsolvating solvents (including fluorinated ethers, fluorinated borate, and fluorinated orthoformate) added in HCEs enable the formation of LHCEs with high-concentration solvation structures. However, low-solvating fluorinated carbonate will coordinate with Li⁺ ions and form a second solvation shell or a pseudo-LHCE which diminishes the benefits of LHCE. In addition, it is evident that the diluent has significant influence on the electrode/electrolyte interphases (EELs) beyond retaining the high-concentration solvation structures. Diluent molecules surrounding the high-concentration clusters could accelerate or decelerate the anion decomposition through coparticipation of diluent decomposition in the EEI formation. The varied interphase features lead to significantly different battery performance. This study points out the importance of diluents and their synergetic effects with the conductive salt and the solvating solvent in designing LHCEs. These systematic comparisons and fundamental insights into LHCEs using different types of fluorinated solvents can guide further development of advanced electrolytes for high-voltage LMBs.

lithium metal batteries | solvation structure | diluent | interphase | LHCE

After decades of dormancy since the emergence of lithium (Li)-ion batteries (LIBs) in the early 1990s, Li metal batteries (LMBs) have been revitalized in recent years as one of the most promising electrochemical energy storage systems because of their high energy densities (1–3). Nevertheless, the renaissance of Li metal anodes (LMAs) used in LMBs is still constrained by two critical obstacles: low coulombic efficiency (CE) and high surface Li growth over cycling. In this regard, the electrolyte has been increasingly recognized as one of the most critical components in stabilizing LMAs and regulating Li deposition and growth because it determines the nature of the solid electrolyte interphase (SEI) on LMAs (4, 5). The state-of-the-art (SOA) LiPF₆/carbonate electrolytes tailored to LIB chemistries have demonstrated good ionic conductivity, electrochemical stability, and favorable SEI properties on graphite anodes (6). Although the overarching design goals of an ideal electrolyte remain the same from LIBs to LMBs, Li metal, with an electrochemical potential of −3.040 V vs. the standard hydrogen electrode, is very reactive to the SOA carbonate electrolytes and leads to severe LMA corrosion and electrolyte depletion. It also

results in uncontrolled Li dendrite growth and greater safety risks for practical applications (5, 7). To this end, electrolytes beyond SOA carbonate electrolytes are essential to enable longer cycle and calendar lives and higher safety of LMBs. Although ethers are known to be more stable with the LMA than the carbonate solvents, their intrinsic instability against oxidation in regular dilute electrolytes has long hindered their applications beyond 4.0 V vs. Li/Li⁺. However, long cycling stability was recently reported in Li||LiNi_{1/3}Mn_{1/3}Co_{1/3}O₂ (NMC111) cells with a charge cutoff voltage of 4.3 V, where an ether-based highly concentrated electrolyte (HCE) was used (8). The HCE of lithium bis(fluorosulfonyl)imide (LiFSI) in 1,2-dimethoxyethane (DME) at a molar ratio of LiFSI:DME = 1:1.2 could greatly enhance the stability of LMBs with a Ni-rich LiNi_{0.8}Mn_{0.1}Co_{0.1}O₂ (NMC811) cathode at 4.4 and 4.5 V, even under practical conditions (9). In this HCE, the absence of free DME

Significance

Lithium (Li) metal battery (LMB) is a very promising candidate for the next-generation high-energy-density batteries. However, its practical applications have been impeded by the instability of metallic Li in the state-of-the-art carbonate electrolytes. Localized high-concentration electrolytes (LHCEs) shed light for practical use of LMBs by generating stable, robust solid electrolyte interphase on Li. Here we investigate various types of fluorinated cosolvents as diluents for LHCEs to understand the correlation between the battery performance and the solvation structure and electrode/electrolyte interfacial chemistry. It clearly reveals that the diluent surrounding the highly concentrated salt-solvating solvent clusters accelerates/decelerates anion decomposition, tunes the properties of interphases, and subsequently influences the battery performance. These results can guide further development of advanced electrolytes for LMBs.

Author contributions: X.C., W.X., and J.-G.Z. designed research; X.C., P.G., X.R., L.Z., M.H.E., B.E.M., J.H., C.N., and D.L. performed research; X.C., P.G., X.R., L.Z., M.H.E., B.E.M., J.H., C.N., D.L., B.W.A., C.W., J.X., J.L., W.X., and J.-G.Z. analyzed data; and X.C., P.G., W.X., and J.-G.Z. wrote the paper.

The authors declare no competing interest.

This article is a PNAS Direct Submission.

Published under the PNAS license.

¹X.C. and P.G. contributed equally to this work.

²Present address: Department of Materials Science and Engineering, University of Science and Technology of China, Hefei 230026, China.

³To whom correspondence may be addressed. Email: wu.xu@pnnl.gov or jiguang.zhang@pnnl.gov.

This article contains supporting information online at <https://www.pnas.org/lookup/suppl/doi:10.1073/pnas.2020357118/-DCSupplemental>.

Published February 25, 2021.

molecules alters the solvation structures of Li^+ and leads to a salt-derived SEI on the LMA and a stable cathode electrolyte interphase (CEI) on the high-voltage cathode. These stable SEI/CEI layers act as kinetic barriers between the electrolyte and the electrodes and thereby limit the continuous side reactions on both LMA and high-voltage cathode during repeated cycling (9). Yamada's group also reported superconcentrated LiFSI/dimethyl carbonate (DMC) electrolytes for high-voltage (5 V) graphite|| $\text{LiNi}_{0.5}\text{Mn}_{1.5}\text{O}_4$ batteries with good cycling durability and rate capability together with enhanced safety (10).

To further advance HCEs, localized high-concentration electrolytes (LHCEs) have been developed by introducing non-solvating or low-solvating solvents (also called diluents) into HCEs (9, 11–13). The LHCEs not only preserve the favorable solvation structures (highly concentrated coordination clusters) in HCEs but also significantly reduce the overall salt concentration in the electrolyte, which is beneficial for lowering the electrolyte viscosity and cost as well as improving the electrolyte wettability on electrodes and separator. Our group previously investigated the effects of a series of model electrolyte solvents (carbonate, sulfone, phosphate, and ether) for LHCEs and revealed the intrinsic synergistic effects between the salt and the solvent when they coexist on electrode surfaces (14). In this work, we will move to another important component in LHCE, which is diluent. The requirements of a diluent have been given in our previous work (11) and summarized in a review article about HCEs by Yamada et al. (15), which include low viscosity, sufficient electrochemical stability, appropriate permittivity, and coordination property (11, 15). Several hydrofluoroethers (HFEs) that meet the above requirements have been introduced as diluents in different HCEs that are based on different conductive salts and solvating solvents, including bis(2,2,2-trifluoroethyl) ether (BTFE) (11, 13, 16–19), 1,1,2,2-tetrafluoroethyl-2,2,3,3-tetrafluoropropyl ether (TTE) (9, 12), 1H,1H,5H-octafluoropentyl 1,1,2,2-tetrafluoroethyl ether, and 2,2,2-trifluoroethyl 1,1,2,2-tetrafluoroethyl ether (20). The formulated LHCEs successfully improve the cell performance of different battery chemistries, which are mainly enabled by the densely deposited Li underneath the favorable salt-derived SEI chemistry. To reveal the fundamental mechanism behind the merits of using diluents in LHCEs, here we carry out systematic studies on the diluents of the known HFEs (including BTFE and TTE as representatives) and beyond including fluorinated carbonate [bis(2,2,2-trifluoroethyl) carbonate (BT FEC)], fluorinated borate [tri(2,2,2-trifluoroethyl) borate (TFEB)], and fluorinated orthoformate [Tris(2,2,2-trifluoroethyl) orthoformate (TFEO)]. The molecular structures are given in *SI Appendix, Fig. S1*. Post-mortem analyses and theoretical simulations are performed to understand the underlying mechanisms for the varied behaviors in the LHCEs based on different types of diluents. It is evident that the diluent has significant influence on the electrode/electrolyte interphases beyond retaining the high-concentration solvation structures. The high concentration of salt anions present in the primary Li^+ solvation sheath is not the only key point in LHCEs. The diluent molecules surrounding the high-concentration clusters could accelerate or decelerate the anion decomposition through coparticipation of diluent decomposition in the SEI formation. Chemistry of a different nature is also found in the CEI formed in different diluents-based LHCEs. The varied interphase features eventually lead to significantly different levels of battery performance. This study points out the importance of diluents and their synergetic effects with the conductive salt and the solvating solvent in designing LHCEs. These systematic comparisons and fundamental insights into LHCEs that are based on different types of diluents can guide further development of advanced electrolytes for high-voltage LMBs.

Results and Discussion

Table 1 lists the key physical properties of the five fluorinated solvents (indicated by D). These solvents are poor in dissolving

LiFSI salt but are highly miscible with the HCE (LiFSI in DME at a molar ratio of 1:1.2 or 1:1.4), so they work as diluents for the HCE. In all these diluents, the highest occupied molecular orbital (HOMO) energy values are lower than that of the DME solvent (HOMO of -7.19 eV) because the diluents have strong electron-withdrawing CF_3 or CF_2 groups, which indicates they have a higher theoretical oxidative stability than the DME solvent. The lowest unoccupied molecular orbital (LUMO) energy values of these diluents are lower than that of the DME solvent (-0.18 eV), indicating they can be reduced earlier than DME and can participate in the SEI formation on the anode. Table 1 also provides the key physical properties of the corresponding LHCEs (indicated by E) based on these diluents (at the molar ratio of LiFSI:DME:diluent = 1:1.2:3 for all diluents except for TFEB; when diluent is TFEB, LiFSI:DME:TFEB is 1:1.4:3). The LHCEs have an overall salt concentration between 1.65 and 1.06 M, varying according to the diluent. Because the molar ratio of LiFSI, DME, and diluent is fixed, a diluent with a higher molecular weight will yield a lower salt concentration in the corresponding LHCE. This overall salt concentration determines the ionic conductivity of the electrolyte, in which the Li^+ ions are conducted by hopping within the salt-solvent clusters and cluster/carrier (solvation shell) diffusion in the LHCEs, and a higher salt concentration leads to a higher ionic conductivity of the LHCE. At room temperature (25°C), the ionic conductivities of these electrolytes are between 4.88 and 1.61 mS cm^{-1} . Similar electrolyte densities (between 1.39 and 1.48 g mL^{-1}) and much lower viscosities (between 2.86 and 4.92 cP at 25°C) than that of HCE (49.2 cP at 30°C) (21) are obtained in all these LHCEs.

Ab initio molecular dynamics (AIMD) simulations were performed to investigate the effects of different fluorinated solvents on the solvation structures (microscopic structures) of the HCE and the five LHCEs. The molecular structures of the electrolyte components are shown in *SI Appendix, Fig. S1*, and snapshots of the HCE and five LHCE structures from AIMD simulations are shown in Fig. 1 A–F. Clearly, the LiFSI salt is uniformly distributed throughout the DME solvent in the HCE. However, high-salt concentration clusters (aggregations) can be seen in Fig. 1 B, C, E, and F with BTFE, TTE, TFEB, and TFEO as diluents in LHCEs, respectively, while much isolated LiFSI is present in the LHCE with BT FEC as diluent, as shown in Fig. 1D. Diluents BTFE, TTE, TFEB, and TFEO evidently preserve the favorable characteristics of HCE (LiFSI-1.2DME), while BT FEC damages the HCE solvation structure to a certain extent. To simplify the electrolyte solvation structures, schematics of HCE and LHCEs are shown in *SI Appendix, Fig. S2*; also, the radial distribution schemes between Li and O atoms in DME solvent, the FSI^- anion, and diluents based on the AIMD simulation trajectories are exhibited in Fig. 1 G–K and summarized in Fig. 1L. Two sharp peaks at 2 \AA in all LHCEs (Fig. 1 G–K) are identified as Li–O in DME (ODME; S for solvent in Fig. 1L) and Li–O in FSI^- (OFSI; A for anion in Fig. 1L).

This indicates that all Li^+ ions are surrounded by DME solvent molecules and FSI^- anions in the first coordination shell (marked as dashed circle in Fig. 1L). This is a result of the strong attractive interaction between Li^+ and DME/ FSI^- . Meanwhile, O atoms in diluent molecules of BTFE (D1), TTE (D2), TFEB (D4), and TFEO (D5) are found to be barely coordinated with Li^+ in these LHCEs (Fig. 1 G, H, J, and K). This demonstrates that these four diluents are outside of the localized high-concentration LiFSI/DME pairs or clusters, as marked in Fig. 1L. BT FEC (D3), an exception, shows two additional peaks at ~ 3.25 and 3.75 \AA (Fig. 1I), which are related to Li–O in BT FEC, suggesting that BT FEC also participates in Li^+ coordination, although it is not in the first solvation shell of the Li^+ ion. A second solvation shell exists in this electrolyte (marked as dash-dotted line in Fig. 1L). As a result, use of BT FEC weakens the solvation structure of the HCE, which decreases the coordination number of the DME and FSI^- in the first shell from 4 in the other LHCE systems

Table 1. Physical properties of the investigated diluents and their corresponding LHCEs

Diluent	BTFE (D1)	TTE (D2)	BT FEC (D3)	TFEB (D4)	TFEO (D5)
D, molecular weight/g mol ⁻¹	182.06	232.07	226.07	307.91	310.11
D, boiling point/°C	62 to 63	93.2	117 to 118	120 to 123	144 to 146
D, flash point/°C	1	27.5	N/A	43	60
D, density/g mL ⁻¹	1.4	1.53	1.51	1.43	1.46
D, viscosity at 25 °C/cP	0.7	1.43	1.69	1.18	1.97
D, fluorine:hydrogen ratio	1.5	2	1.5	1.5	1.5
D, HOMO/eV	-8.76	-9.31	-9.28	-9.27	-8.84
D, LUMO/eV	-0.5	-0.5	-0.6	-0.47	-0.4
E, salt concentration/M	1.65	1.49	1.49	1.17	1.15
E, density/g mL ⁻¹	1.39	1.48	1.45	1.43	1.41
E, viscosity at 25 °C/cP	2.86	4.92	4.06	2.84	4.86
E, conductivity at 25 °C/mS cm ⁻¹	4.88	2.44	2.64	1.88	1.61

D refers to diluent, E refers to corresponding LHCE, and the HOMO and LUMO values were calculated for the pure fluorinated solvents.

(SI Appendix, Fig. S3 A, B, D, and E) to 1.5 (SI Appendix, Fig. S3C). Therefore, free DME molecules that are not closely coordinated with Li⁺ still exist in this BT FEC-based LHCE, making it a pseudo-LHCE. From the solvation structure point of view, the noncoordinating diluent molecules, including BT FE, TTE, TFEB, and TFEO, are good diluent candidates for the LHCE, while the low-coordination diluent BT FEC is not a good diluent.

Beyond the physical properties of the LHCEs based on different diluents, the influences of diluents on the LMA and the battery performance are significant. Because LHCEs have different solvation structures as described above, the conduction band minimum (CBM) varies in different LHCEs. As shown in projected density of states (PDOS) plots (SI Appendix, Fig. S4 A–E), the CBM in the BT FEC-based LHCE is on BT FEC while the CBMs in the other LHCEs are on the FSI⁻ anion, implying that the FSI⁻ anions are predominantly reduced in all LHCEs except for BT FEC-LHCE. This predominant FSI⁻ decomposition leads to LiFSI-derived SEI formation and has strong effects on Li deposition. Fig. 2 shows scanning electron microscopy (SEM) morphologies of the deposited Li (1 mAh cm⁻² Li deposited on a copper [Cu] substrate at a current density of 0.5 mA cm⁻²) in the studied LHCEs as well as the SOA electrolyte (1 M LiPF₆ in EC-EMC [3:7 by wt.] + 2 wt. % vinylene carbonate). Unlike the severe Li dendrite formation in the SOA electrolyte (Fig. 2A), much larger Li particles are found in all the LHCEs with varied details (Fig. 2B–F). In the BT FEC-LHCE (Fig. 2D), the size of deposited Li is not uniform, and certain small particles (close to dendrite morphology) grow along with the large particles. In TFEB-LHCE (Fig. 2E), apparent defects are observed on the large granular particles. The desired Li morphologies are seen in the LHCEs with BT FE, TTE, or TFEO as diluent; the deposited Li in these electrolytes are large and smooth (Fig. 2B, C, and F). The Li deposition morphologies greatly influence the Li CEs. As shown in Fig. 3A, the SOA electrolyte yields a low average CE of 89.8% as a result of dendrite formation and severe side reactions with Li metal. In the LHCEs, much better CE is attributed to the large size of the Li deposited on Cu. In particular, very high CEs of 99.4, 99.5, and 99.5% are obtained in three LHCEs with diluents of BT FE, TTE, and TFEO, respectively.

When a Li anode was paired with a high-voltage, Ni-rich NMC811 cathode as Li||NMC811 batteries to produce a high-energy-density battery, the cell performance is shown in Fig. 3C–E. A somewhat high specific capacity of 217 mAh g⁻¹ is obtained in the SOA electrolyte in the first cycle for formation at C/10 (Fig. 3C), followed by LHCE-BT FE at 211 mAh g⁻¹ and the rest of the LHCEs at ~200 mAh g⁻¹. For the first cycle at C/3 after formation cycles, the same trend is observed with a specific capacity of 210 mAh g⁻¹ for SOA, 206 mAh g⁻¹ for LHCE-BT FE, and

~200 mAh g⁻¹ for the other LHCEs. A small overpotential difference of ~0.05 V is observed in the cells using these electrolytes, in the order of SOA < LHCE-BT FE < LHCE-BT FEC ~ LHCE-TTE < LHCE-TFEB < LHCE-TFEO. This is closely related to the electrolyte conductivity shown in Table 1 because of the overall salt concentration difference among the LHCEs at the same LiFSI/DME/diluent ratio by mol. The cycling performance of Li||NMC811 cells in different LHCEs is compared in Fig. 3E. As we have reported previously, the SOA electrolyte yields poor cycle life of cells when paired with thin Li (50 μm), although much longer cycle life was obtained and reported when it was paired with thick Li (450 μm or even thicker) (21). With a threshold of 80% capacity retention, the stable cycle numbers of Li||NMC811 with different LHCEs have the following order: 300 (LHCE-TFEO) > 262 (LHCE-TTE) > 162 (LHCE-BT FE) > 50 (LHCE-BT FEC) > 40 (SOA electrolyte) > 32 (LHCE-TFEB). For the LHCE-BT FEC, poor cycle life could be explained mainly by the pseudo-LHCE nature as described in the above section, which is in a lack of high-concentration clusters and the presence of free DME solvent molecules in the electrolyte. Therefore, it behaves similarly to the SOA electrolyte. As for the cell with LHCE-TFEB, even shorter cycle life than that with the SOA electrolyte is observed. This behavior can be attributed to the low Li CE of 95.4%, while the underlying reason could possibly be related to the highly electron-deficient nature of TFEB, which will be discussed in more detail later. As for the LHCE-BT FE, LHCE-TTE, and LHCE-TFEO electrolytes without free DME molecules and with great Li CEs, Li||NMC811 cells show significantly improved cycling performance with a high average cell CE reaching 99.7 and 99.8% over cycling. Electrochemical impedance spectroscopy (EIS) was carried out to monitor the resistance after 100 cycles. The Nyquist plots obtained are compared in Fig. 3B. It is clear that the cells failing quickly (in SOA electrolyte, LHCE-BT FEC, and LHCE-TFEB) have much stronger resistance to Li⁺ diffusion in SEI at high frequency, which is likely a result of the high reactivity between Li metal and these electrolytes. Meanwhile, much smaller resistances are found in the LHCE-BT FE, LHCE-TTE, and LHCE-TFEO, following the order of LHCE-BT FE ~ LHCE-TTE < LHCE-TFEO, consistent with the overpotentials shown in Fig. 3D.

To further reveal the diluent effect in the Li||NMC811 cells, the cycled LMAs and NMC811 cathodes were collected to seek a better understanding of the interfacial chemistries, including SEI on the LMA and CEI on the NMC811 cathode. In recent studies, various HCEs and LHCEs have been used in LMBs and demonstrated much better LMB stability than conventional electrolytes by generating salt-derived SEIs (21–23). Nevertheless, little attention has been paid to the role of the diluent. Here X-ray photoelectron spectroscopy (XPS) analysis was performed to

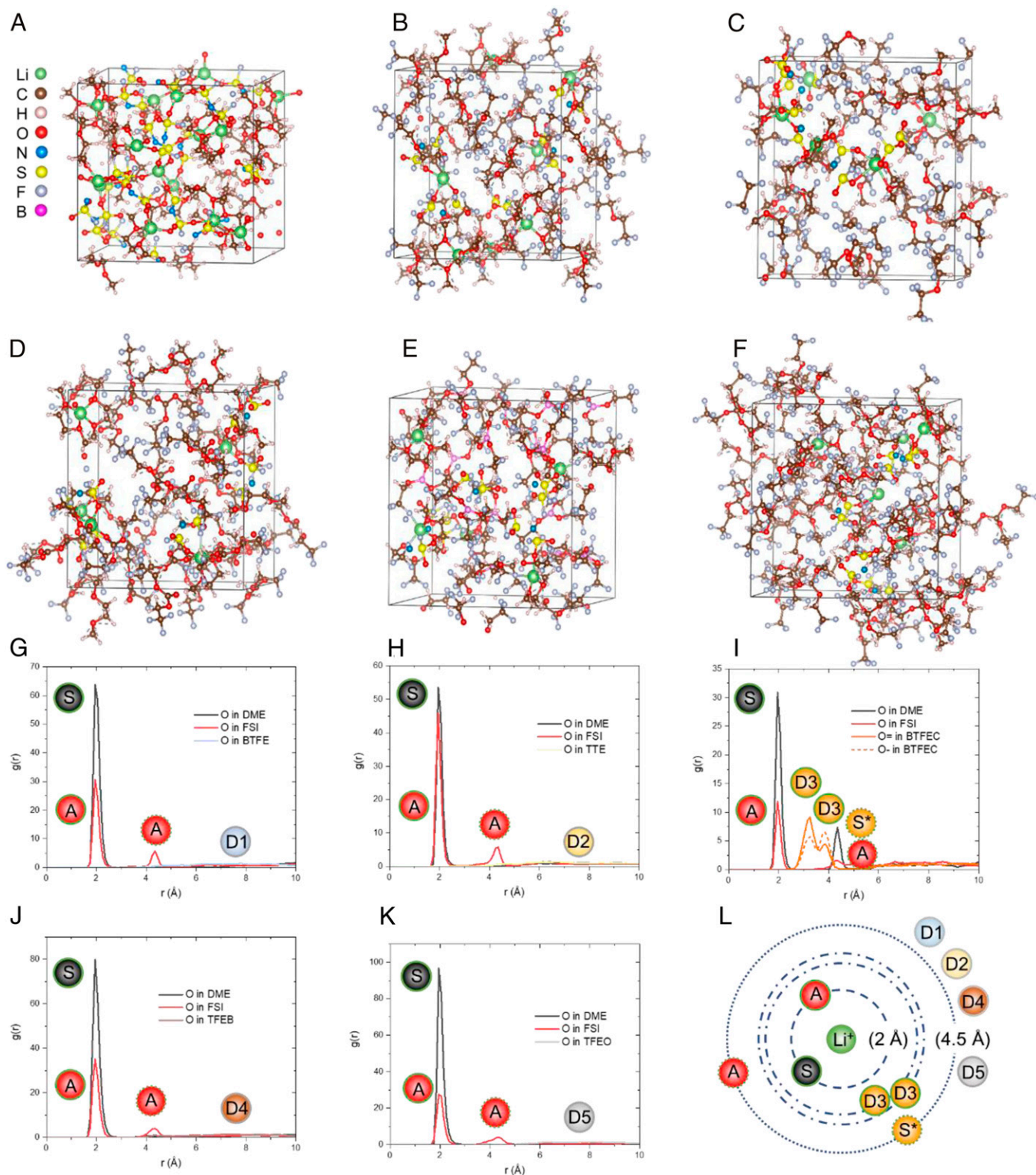


Fig. 1. AIMD simulation snapshots of (A) HCE and LHCEs with (B) BTFE, (C) TTE, (D) BT FEC, (E) TFEB, and (F) TFEO as diluent. Detailed radial distribution of LHCEs with (G) BTFE, (H) TTE, (I) BT FEC, (J) TFEB, and (K) TFEO as diluent. D1 to D5 are defined in Table 1. S, solvent; A, anion. (L) Schematic illustration of the radial distribution of LHCEs listed in Table 1. The green outline on circles in G–L means the coordination between the specific item to the Li^+ ion, the solid line indicates relatively strong coordination, and dotted line indicates the relatively weak coordination.

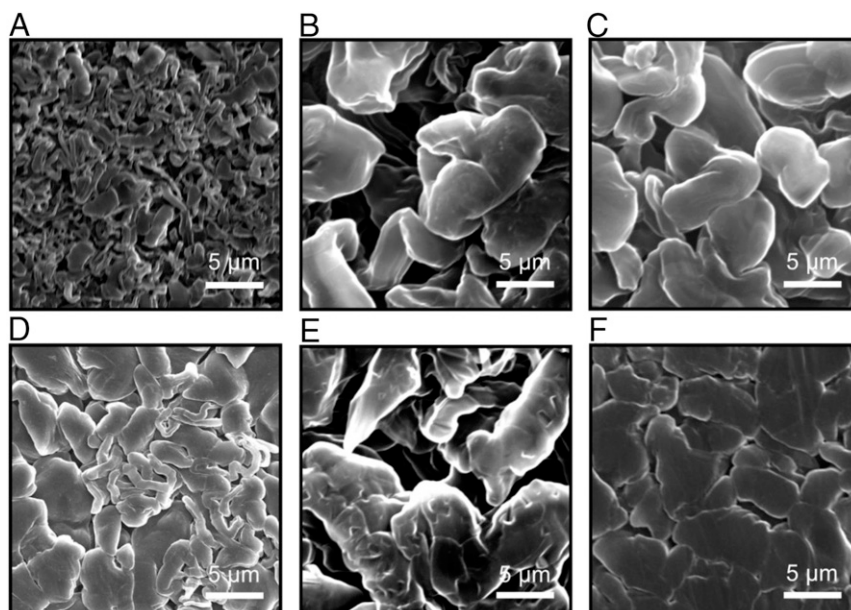


Fig. 2. SEM images of deposited Li morphologies in the (A) SOA electrolyte and LHCEs with (B) BTFE, (C) TTE, (D) BT FEC, (E) TFEB, and (F) TFEO as diluent.

characterize the compositions of SEIs formed in LHCEs with different diluents.

Fig. 4A summarizes elemental distributions at different depths in the SEIs, and Fig. 4 B–E show C 1s, S 2p, N 1s, and F 1s spectra as representatives for detailed composition analysis. Five significant trends are identified in Fig. 4. 1) In all LHCEs, the SEIs have high contents of inorganic species derived from salt, as indicated by the high contents of Li, O, and/or F elements. In LHCEs with diluents of TTE and TFEO, Li and O constitute an atomic ratio of more than 80%. The BTFE-LHCE has Li and O combined at about 60% and F at about 20%, while much more Li and F are found in BT FEC-LHCE (70%) and TFEB-LHCE (40%) together with around 20% O. Fig. 4 C–E for S 2p, N 1s, and F 1s demonstrate the decomposition of LiFSI; partial LiFSI is almost completely reduced in LHCEs with TTE and TFEO due to the higher intensity of S^{2-} and S_n^{2-} species. 2) As indicated by the C atomic ratio and C 1s spectra, solvent/diluent molecules are still involved in the SEI formation, although SEIs are mainly derived from the LiFSI in these LHCEs. BT FEC-LHCE has the highest C atomic ratio (20%) among the five different diluent-based LHCEs. It suggests the most severe solvent/diluent decomposition in this electrolyte, which agrees with the PDOS results obtained in AIMD simulation, as mentioned in an earlier section. It can be strongly related to the pseudo-LHCE nature of BT FEC-LHCE. 3) An additional peak at 293 eV (CF_3) in LHCEs with BT FEC and TFEB also proves that diluents BT FEC and TFEB have strong interactions with the LMA. The B content (5%) in TFEB-LHCE further confirms that TFEB takes part in the SEI formation. 4) The transition metal Ni is found on the Li surface after cycling in the TFEB-LHCE, indicating the TFEB-LHCE is highly reactive with the cathode as well, which leads to a transition metal dissolution and migration to the LMA. This will be further discussed in the next section on cathode analysis. 5) According to the atomic ratio distribution at different depths shown in Fig. 4A, LHCEs with TTE and TFEO have the most uniform elemental distribution along the thickness of the SEI, suggesting very uniform SEIs in these two electrolytes. We can conclude that varied degrees of reactivity between diluent and LMA exist in LHCEs with different diluents, and homogeneous Li_2O_x -rich SEIs in LHCEs with TTE and TFEO

are favorable for LMA stability and result in high CE (Fig. 3A) and long cycling in Li||NMC811 cells (Fig. 3E).

In addition, the diluent selection is also closely related to the reactions between the electrolyte and the active cathode. To elucidate the interfacial reactions, XPS was also used to characterize the CEIs on NMC811 cathodes after 100 cycles. Fig. 5A shows the atomic ratios of the elements found on cathodes cycled in different LHCEs, and their regional spectra are shown in Fig. 5 B–E. Three major points can be summarized as follows. 1) In four LHCEs with BTFE, BT FEC, TTE, and TFEO as diluent, LiF is dominant in the CEIs, as demonstrated by the high Li and F contents as well as the F1s peak at 685 eV (Fig. 5E). 2) Considering S 2p (Fig. 5C) and N 1s (Fig. 5D) spectra with much higher intensity of NSO_xF_y in LHCEs with BTFE, TTE, and TFEO, more LiFSI decomposition takes place in these LHCEs and helps form LiF in these electrolytes. On the other hand, LiF generation in BT FEC-LHCE is mainly derived from the decomposition of BT FEC, as suggested by the limited LiFSI decomposition in this electrolyte. 3) Severe TFEB decomposition occurs in the TFEB-LHCE as evidenced by the very high content of C (40 to 50%) and B (30 to 10%) from surface to bottom of the CEI, as shown in Fig. 5A.

The cycled cathodes were also characterized by annular bright-field scanning transmission electron microscopy (ABF-STEM) and high-angle annular dark-field (HAADF)-STEM to study the cathode structures and the morphology of CEIs formed in different LHCEs. As shown in Fig. 5 F–O, in the BTFE-LHCE, a CEI layer thinner than 2 nm covers the NMC811 (Fig. 5F), and the surface of the cathode particle developed a cation-mixing phase structure with a thickness around 2 nm (Fig. 5K). This phase transformation from the initial layered structure (9, 21) is likely due to corrosion of the electrolyte, and oxygen vacancies left by interfacial reactions would trigger more Li^+/Ni^{2+} mixing in the interlayer (24). Moreover, the oxygen vacancies preferentially diffuse along {104} planes, subsequently facilitating the cation-mixing phase growth (Fig. 5K) (24). In TTE-LHCE, a somewhat thicker CEI (3 nm) is observed (Fig. 5G), but a much thinner cation-mixing layer of 1 nm without bulk corrosion can be seen in Fig. 5L. In TFEO-LHCE, an even thicker CEI of 5 nm is obtained on the NMC cathode, which successfully suppresses

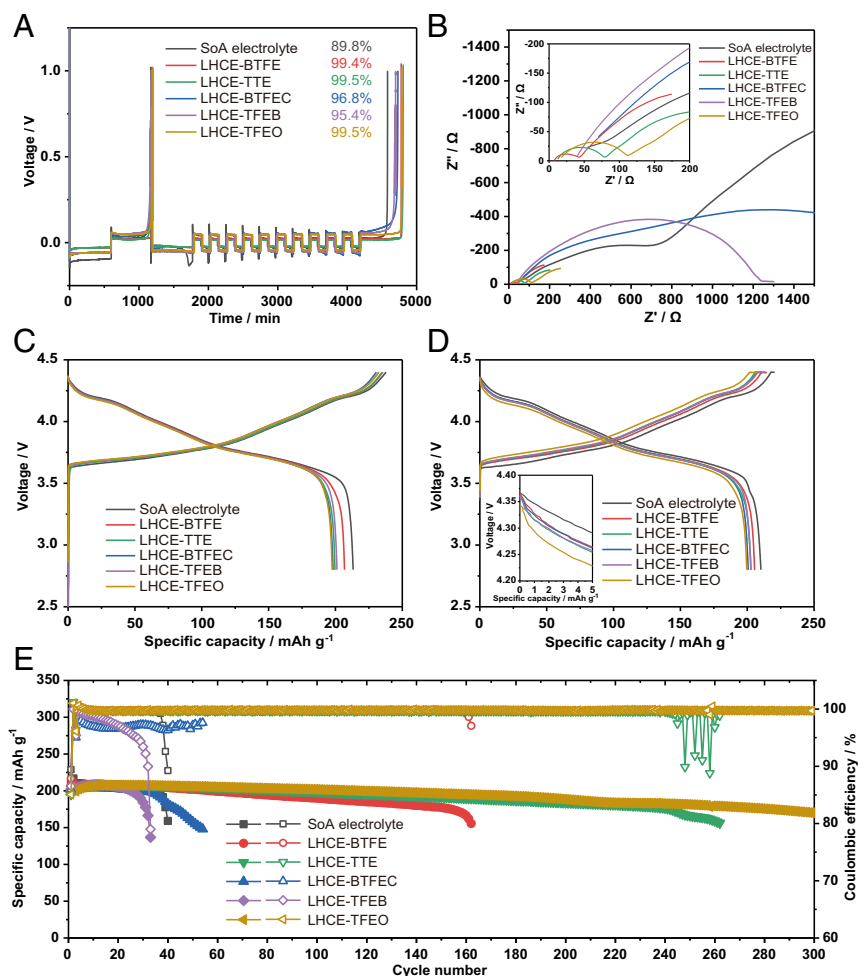


Fig. 3. Electrochemical properties of the LHCEs based on different diluents compared to those of the SoA electrolyte. (A) Li CE, (B) EIS spectra after 100 cycles in Li||NMC811 cells, (C) initial charge/discharge curves of the Li||NMC811 cells at C/10 for formation, (D) charge/discharge curves of the Li||NMC811 cells at C/3 after two formation cycles, and (E) long-term cycling stability.

the cation-mixing phase transition. For these LHCEs, the CEI thickness and LiF crystallinity follow the order of BTFE < TTE < TFEO, and the suppression of cation-mixing transformation

follows the same order, which is also in good agreement with the cell capacity retention trend shown in Fig. 3E. The significant amount of LiF found on these cathode primary particles

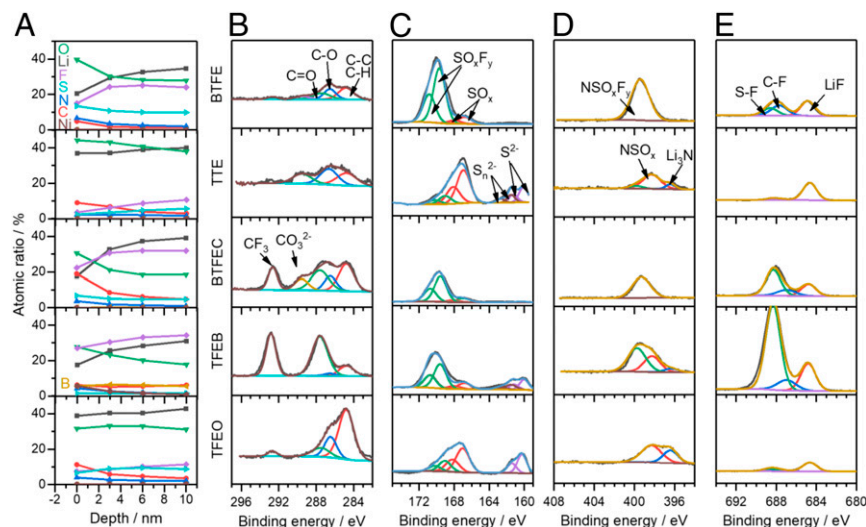


Fig. 4. (A) The XPS atomic ratios of different elements at different depths on cycled Li anodes using different LHCEs. The regional XPS spectra for selected elements on cycled Li anodes: (B) C 1s, (C) S 2p, (D) N 1s, and (E) F 1s.

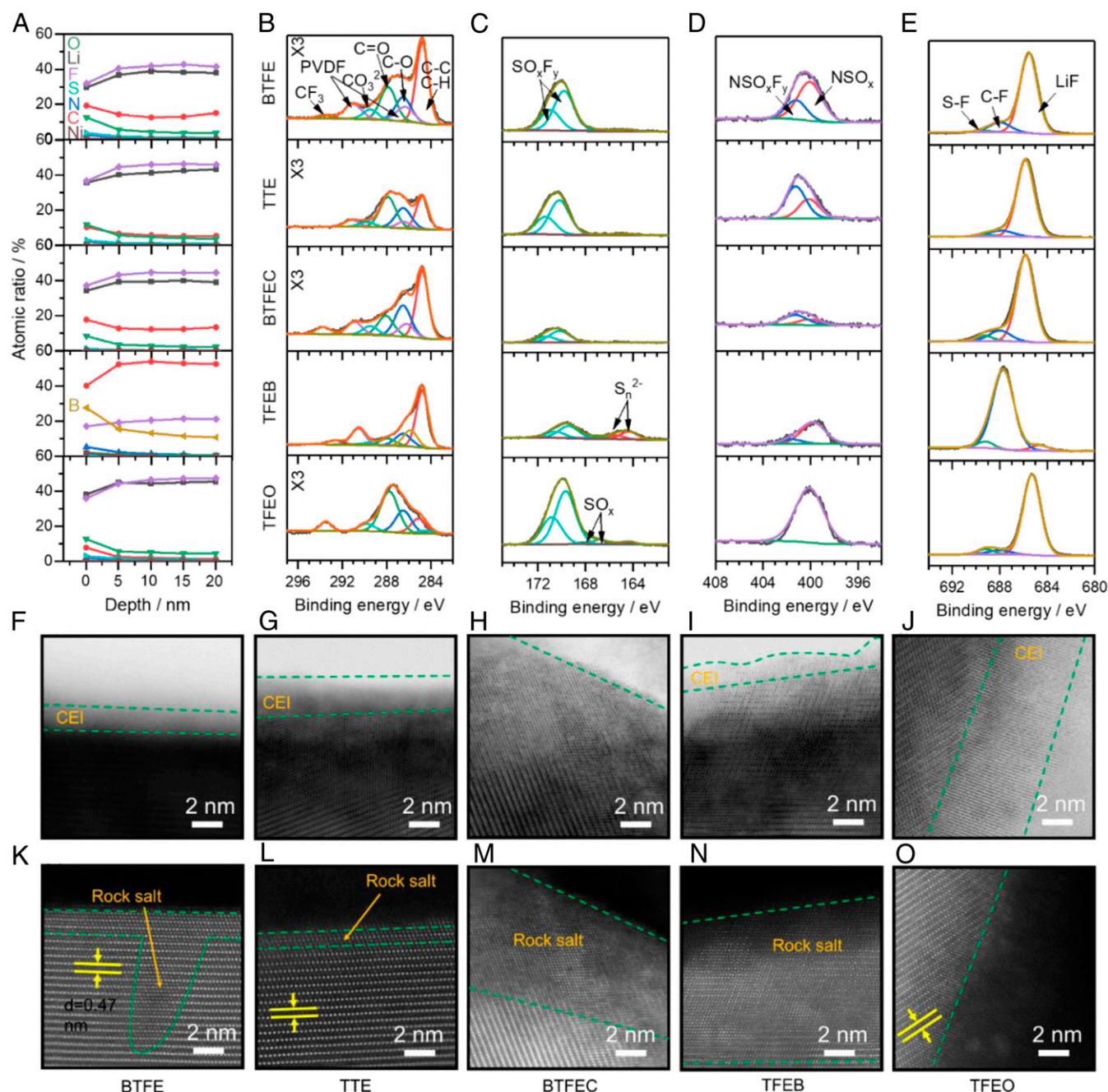


Fig. 5. (A) The XPS atomic ratios of different elements at different depths on cycled NMC811 cathodes using different LHCEs. The regional XPS spectra for selected elements on cycled NMC811 cathodes: (B) C 1s, (C) S 2p, (D) N 1s, and (E) F 1s. (F–J) The HAADF-STEM images and (K–O) the ABF-STEM images of NMC811 cathodes after 100 cycles in different LHCEs.

supports previous findings about the critical role of LiF in CEI for effective interfacial protection (9, 21). With the strong protection of a LiF-rich layer, no apparent transition metal (represented by Ni) dissolution and transport to the cycled LMA is observed in these electrolytes (Fig. 4A). As for BT FEC-LHCE, a 6- to 8-nm Li⁺/Ni²⁺ mixing layer exists on the NMC811 surface (Fig. 5M) because of the lack of CEI protection (Fig. 5H) on the NMC811 primary particles. In TFEB-LHCE, an even thicker layer of 10 to 14 nm phase change is observed (Fig. 5N), suggesting that severe cathode corrosion occurs. It is probably caused by the electron-deficient nature of TFEB that accelerates the oxygen release in Ni-rich NMC and accounts for a fast cathode decay. In addition to the stable molecular configurations, transient and kinetic

aspects also play important roles in the interactions between the electrolyte and electrode, which need further investigation relying on the development of more advanced in situ technologies.

Conclusion

Different types of fluorinated solvents, including fluorinated ethers (BTFE and TTE), fluorinated carbonate (BT FEC), fluorinated borate (TFEB), and fluorinated orthoformate (TFEO), were investigated as diluents in LHCEs for rechargeable LMBs in this work. Significant differences were observed in the LHCEs (based on LiFSI-1.2DME HCE) with these diluents. Among them, BT FEC coordinates with Li⁺ in a second solvation shell beyond the first solvation with DME and FSI⁻, which partially damages

the high-concentration coordinated clusters in the HCE by forming a pseudo-LHCE; thus, the favorable features of HCE are lost in BTfEC-LHCE. LHCEs with BTfE, TTE, TFEB, and TFEo maintain the high-concentration salt clusters while the overall LiFSI concentration decreases in these electrolytes. In addition to the crucial role of the FSI[−] anion in the SEI and CEI properties in LHCEs, the diluent molecules also make great contributions to the interfacial chemistries on both the cathode and the anode. TFEB significantly accelerates oxygen release in the Ni-rich NMC811 material and causes fast cathode decay because of its electron-deficient nature. BTfE-, TTE-, and TFEo-based LHCEs demonstrated high Li CE of 99.4, 99.5, and 99.5%, respectively. For these three LHCEs, the high-voltage Li||NMC811 cell performance was determined by the CEI chemistries under the testing conditions. The capacity retention of Li||NMC811 with the tested LHCEs follows the order of TFEo-LHCE > TTE-LHCE > BTfE-LHCE > BTfEC-LHCE > SOA electrolyte > TFEB-LHCE. This work provides insight for designing LHCEs and highlights the selection rules for diluents to achieve stable cycling of high-voltage LMBs.

Materials and Methods

Materials. Battery-grade LiFSI was received from Nippon Shokubai and was used after vacuum drying at 120 °C for 24 h. DME (battery grade) was purchased from Gotting, Inc., and used as received. BTfE, TTE, BTfEC, TFEB, and TFEo were purchased from SynQuest Laboratories and were dried with preactivated molecular sieves before use. Electrolytes were prepared by dissolving LiFSI in DME solvent and then mixing with the diluents at desired ratios. Cathode material, Ni-rich NMC811, was purchased from Targray. Cathode laminate with an areal capacity loading of about 1.5 mAh cm^{−2} was prepared by coating Al foil with a cathode slurry containing 96% NMC811 material, 2% conductive carbon (C-ENERGY Super P C65), and 2% PVDF binder (Kureha L#1120) in N,N-dimethylpyrrolidinone. Cathode disks were punched with a diameter of 1.27 cm. The LMA was Li (50 μm) on Cu foil ordered from China Energy Lithium Co., Ltd.

Electrochemical Tests. For Li CE tests, Li||Cu cells were assembled inside an argon-filled glovebox (MBraun, H₂O < 1 ppm, O₂ < 1 ppm). Li foil, polyethylene (PE) separator (Asahi Kasei), and Cu foil were sandwiched together in CR2032-type (MTI) cells and sealed with 75 μL electrolyte. The Li CE was tested using the CE protocol (method 3 with Q_T of 5 mAh cm^{−2}, Q_C of 1 mAh cm^{−2}, and *n* of 10) reported in the previous work (25). Li||Cu cells were also used for Li deposition, with 1 mAh cm^{−2} Li deposited on Cu at a current of 0.5 mA cm^{−2}, and Li on Cu foil was collected for morphology examination. The Li||NMC811 cells were assembled in the same way but replacing the Cu foil with an NMC811 cathode disk, and an Al-clad cathode case was used to avoid stainless steel corrosion at high voltages. Another Al foil with a diameter of 1.9 cm was placed between the cathode disk and the Al-clad case for further protection. The cells were charged/discharged in a voltage window of 2.8 to 4.4 V on Land battery testers (Wuhan Land) at 25 °C and at C/3 rate (a constant-voltage charge at 4.4 V was applied after the cell was charged to 4.4 V until the current reached C/20 or the time reached 1 h) after two formation cycles at C/10. EIS measurements were carried out on Li||NMC811 cells to monitor the resistance after 100 cycles. AC impedance spectra were recorded in potentiostatic mode on a CHI 660 electrochemical workstation in a frequency range of 100 kHz to 10 mHz with a 5-mV perturbation at 25 °C and at the open circuit voltage at 0% state of charge.

Characterizations. The electrolyte viscosity (η) was measured on a Brookfield DV-II+ Pro Viscometer at 25 °C (20). The ionic conductivity of the electrolytes was measured with a fully integrated multichannel conductivity spectrometer (Bio-Logic MCS10) (21). For postmortem analyses, the cycled cells were disassembled inside the argon-filled glovebox to collect cycled electrodes. The electrodes were then rinsed with DME solvent to remove residual electrolytes, dried under vacuum, and transferred in airtight vessels for XPS, SEM, and STEM measurements. The XPS measurements were conducted on a Physical Electronics Quantera scanning X-ray microprobe with a focused monochromatic Al K_α X-ray source (21). For depth profiling, the samples were sputtered with argon ions at 2 kV, 0.5 mA, and 45° incident angle, and the sputter rates were based on the sputter rate calibrated from a known thickness of SiO₂, which was 6.1 nm min^{−1} (21). The STEM samples were prepared on an FEI Helios Dual Beam system. An ~2 μm Pt layer was coated on a targeted particle that was selected randomly from cycled NMC811 for the lift-out process and was then extracted along with the capping layers and welded to the TEM grid (24). The thinning processes were conducted at 30 kV, followed by a 5 kV and then a 2 kV Ga-ion beam to polish the surface and remove the damaged layers (24). The as-prepared sample was then characterized on a JEOL JEM-ARM200CF spherical aberration-corrected microscope with the convergence angle at 20.6 mrad for imaging; the signals at 90 to 370 mrad were collected for HAADF-STEM, and the ones at 10 to 23 mrad were collected for ABF-STEM imaging (24).

AIMD Simulation. AIMD simulations were performed using the Vienna Ab initio Simulation Package. Electron-ion interactions were described by the projector-augmented wave pseudopotentials (26) with a cutoff energy of 400 eV. The exchange-correlation functional was represented using the Perdew–Burke–Ernzerhof generalized gradient approximation. An exchange-correlation functional with a Gaussian smearing width term of 0.05 eV was used. The convergence criteria for electronic self-consistent iteration was set to 1 × 10^{−5} eV. The effects of various diluents in LHCEs were investigated in the canonical ensemble. The initial densities of these systems and their molar ratios are listed in Table 1. The temperature of the AIMD simulation systems was kept constant using the Nosé thermostat method with a Nosé-mass parameter of 0.1 at 298 K. The initial structure of each LiFSI-DME-diluent system was set up by randomly placing numbers of LiFSI, DME, and diluent molecules based on experimental densities and molar ratios. These initial geometry structures were first optimized with classical molecular dynamics using the all-atom optimized potentials for liquid simulations (OPLS-AA) force field (27). Then the systems were preequilibrated for 5 ps by AIMD. Finally, product simulations of 10 ps were carried out with a time step of 1 fs. The PDOS were calculated and averaged over 10 different configurations (extracted from MD simulation snapshots) to represent an ensemble average of the PDOS. A Monkhorst-Pack k-point mesh grid scheme was used with dimensions of 2 nm × 2 nm × 2 nm.

Data Availability. All study data are included in the article and [SI Appendix](#).

ACKNOWLEDGMENTS. This work was supported by the Assistant Secretary for Energy Efficiency and Renewable Energy, Vehicle Technologies Office, of the US Department of Energy (DOE) through the Advanced Battery Materials Research program (Battery500 Consortium) under contract no. DE-AC05-76RL01830. The SEM, TEM, and XPS were performed at the Environmental Molecular Sciences Laboratory (grid.436923.9), a DOE Office of Science User Facility sponsored by the Office of Biological and Environmental Research and located at Pacific Northwest National Laboratory (PNNL). PNNL is operated by Battelle for the DOE under contract DE-AC05-76RL01830. The LiFSI salt was provided by Dr. Kazuhiko Murata of Nippon Shokubai Co., Ltd.

1. W. Xu et al., Lithium metal anodes for rechargeable batteries. *Energy Environ. Sci.* **7**, 513–537 (2014).
2. X.-B. Cheng, R. Zhang, C.-Z. Zhao, Q. Zhang, Toward safe lithium metal anode in rechargeable batteries: A review. *Chem. Rev.* **117**, 10403–10473 (2017).
3. D. Lin, Y. Liu, Y. Cui, Reviving the lithium metal anode for high-energy batteries. *Nat. Nanotechnol.* **12**, 194–206 (2017).
4. K. Xu, Electrolytes and interphases in Li-ion batteries and beyond. *Chem. Rev.* **114**, 11503–11618 (2014).
5. J.-G. Zhang, W. Xu, J. Xiao, X. Cao, J. Liu, Lithium metal anodes with nonaqueous electrolytes. *Chem. Rev.* **120**, 13312–13348 (2020).
6. K. Xu, Nonaqueous liquid electrolytes for lithium-based rechargeable batteries. *Chem. Rev.* **104**, 4303–4417 (2004).
7. M. Li, C. Wang, Z. Chen, K. Xu, J. Lu, New concepts in electrolytes. *Chem. Rev.* **120**, 6783–6819 (2020).
8. S. Jiao et al., Stable cycling of high-voltage lithium metal batteries in ether electrolytes. *Nat. Energy* **3**, 739–746 (2018).
9. X. Ren et al., Enabling high-voltage lithium-metal batteries under practical conditions. *Joule* **3**, 1662–1676 (2019).
10. J. Wang et al., Superconcentrated electrolytes for a high-voltage lithium-ion battery. *Nat. Commun.* **7**, 12032 (2016).
11. S. Chen et al., High-voltage lithium-metal batteries enabled by localized high-concentration electrolytes. *Adv. Mater.* **30**, e1706102 (2018).
12. X. Ren et al., Localized high-concentration sulfone electrolytes for high-efficiency lithium-metal batteries. *Chem* **4**, 1877–1892 (2018).
13. S. Chen et al., High-efficiency lithium metal batteries with fire-retardant electrolytes. *Joule* **2**, 1548–1558 (2018).
14. X. Ren et al., Role of inner solvation sheath within salt-solvent complexes in tailoring electrode/electrolyte interphases for lithium metal batteries. *Proc. Natl. Acad. Sci. U.S.A.* **117**, 28603–28613 (2020).
15. Y. Yamada, J. Wang, S. Ko, E. Watanabe, A. Yamada, Advances and issues in developing salt-concentrated battery electrolytes. *Nat. Energy* **4**, 269–280 (2019).

16. L. Yu *et al.*, A localized high-concentration electrolyte with optimized solvents and lithium difluoro(oxalate)borate additive for stable lithium metal batteries. *ACS Energy Lett.* **3**, 2059–2067 (2018).
17. J. Zheng *et al.*, Extremely stable sodium metal batteries enabled by localized high-concentration electrolytes. *ACS Energy Lett.* **3**, 315–321 (2018).
18. X. Cao *et al.*, Nonflammable electrolytes for lithium ion batteries enabled by ultra-conformal passivation interphases. *ACS Energy Lett.* **4**, 2529–2534 (2019).
19. H. Jia *et al.*, High-performance silicon anodes enabled by nonflammable localized high-concentration electrolytes. *Adv. Energy Mater.* **9**, 1900784 (2019).
20. J. Zheng *et al.*, High-fluorinated electrolytes for Li-S batteries. *Adv. Energy Mater.* **9**, 1803774 (2019).
21. X. Cao *et al.*, Monolithic solid–electrolyte interphases formed in fluorinated orthoformate-based electrolytes minimize Li depletion and pulverization. *Nat. Energy* **4**, 796–805 (2019).
22. J. Qian *et al.*, High rate and stable cycling of lithium metal anode. *Nat. Commun.* **6**, 6362 (2015).
23. L. Suo *et al.*, Fluorine-donating electrolytes enable highly reversible 5-V-class Li metal batteries. *Proc. Natl. Acad. Sci. U.S.A.* **115**, 1156–1161 (2018).
24. L. Zou *et al.*, Solid–liquid interfacial reaction triggered propagation of phase transition from surface into bulk lattice of Ni-rich layered cathode. *Chem. Mater.* **30**, 7016–7026 (2018).
25. B. D. Adams, J. Zheng, X. Ren, W. Xu, J.-G. Zhang, Accurate determination of coulombic efficiency for lithium metal anodes and lithium metal batteries. *Adv. Energy Mater.* **8**, 1702097 (2018).
26. G. Kresse, D. Joubert, From ultrasoft pseudopotentials to the projector augmented wave method. *Phys. Rev. B Condens. Matter Mater. Phys.* **59**, 1758–1775 (1999).
27. W. L. Jorgensen, D. S. Maxwell, J. Tirado-Rives, Development and testing of the OPLS all-atom force field on conformational energetics and properties of organic liquids. *J. Am. Chem. Soc.* **118**, 11225–11236 (1996).